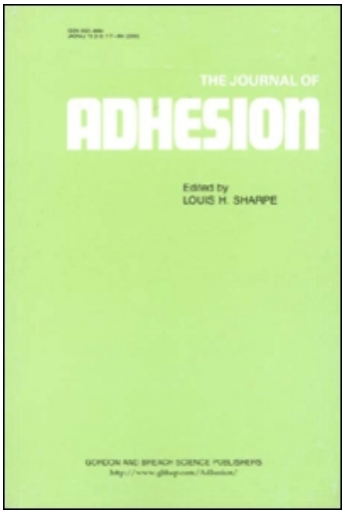

The Journal of Adhesion
Publication details, including instructions for authors and subscription information:
http://www.informaworld.com/smpp/title~content=t713453635

Engineering Therapeutic Nanocarriers with Optimal Adhesion for Targeting

Jered B. Haun[a]; Gregory P. Robbins[b]; Daniel A. Hammer[ab]
[a] Department of Bioengineering, University of Pennsylvania, Philadelphia, Pennsylvania, USA [b] Department of Chemical and Biomolecular Engineering, University of Pennsylvania, Philadelphia, Pennsylvania, USA

Online publication date: 05 February 2010

To cite this Article Haun, Jered B. , Robbins, Gregory P. and Hammer, Daniel A.(2010) 'Engineering Therapeutic Nanocarriers with Optimal Adhesion for Targeting', The Journal of Adhesion, 86: 1, 131 — 159
To link to this Article: DOI: 10.1080/00218460903510414
URL: http://dx.doi.org/10.1080/00218460903510414

The Journal of Adhesion, 86:131–159, 2010

ISSN: 0021-8464 print/1545-5823 online
DOI: 10.1080/00218460903510414

Taylor & Francis
Taylor & Francis Group

Engineering Therapeutic Nanocarriers with Optimal Adhesion for Targeting

Jered B. Haun[1], Gregory P. Robbins[2], and Daniel A. Hammer[1,2]
[1]Department of Bioengineering, University of Pennsylvania, Philadelphia, Pennsylvania, USA
[2]Department of Chemical and Biomolecular Engineering, University of Pennsylvania, Philadelphia, Pennsylvania, USA

There is considerable interest in developing therapeutic delivery carriers that can be targeted via *receptor-ligand interactions to sites within the blood stream. The adhesion of carriers is determined by the combined effects of transport phenomena, hydrodynamic force, and the dynamics of multivalent receptor/ligand bonding. Optimizing the adhesion of carriers requires developing relationships between these factors and carrier properties such as size and receptor coating density. Recently, we developed canonical relationships for the binding of antibody-conjugated 200 nm particles to surfaces coated with a vascular adhesion molecule, intercellular adhesion molecule-1. Here we extend our previous studies of adhesion to particles of different size, including 40 nm and 1 μm particles. Particle binding is assessed under fluid flow in a parallel plate flow chamber while varying particle receptor density, substrate ligand density, and flow rate. Using a stochastic simulation and transport-reaction model we then extract multivalent kinetic rate constants for particle attachment and detachment from the binding data. We demonstrate that particles go though a maximum in binding with particle size. For small particles, increasing size increases receptor-ligand encounter rates; for larger particles, fluid shear force begins to dominate, leading to higher forces and decreased adhesion. Our methods provide a means for optimizing particle size and receptor density for the selective binding of particles to vascular endothelium under flow.*

Keywords: Cardiovascular drug delivery; ICAM-1; Molecular targeting; Multivalent kinetics; Nanoparticle adhesion; Targeted delivery carriers

Received 23 January 2009; in final form 24 November 2009.

One of a Collection of papers honoring J. Herbert Waite, the recipient in February 2009 of *The Adhesion Society Award for Excellence in Adhesion Science, Sponsored by 3 M*.

Address correspondence to Daniel A. Hammer, Skirkanich Hall, 240S Skirkanich, 210 South 33rd Street, Philadelphia, PA 19104, USA. E-mail: hammer@seas.upenn.edu

INTRODUCTION

Understanding the adhesive behavior of nano-scale colloidal materials is critical for optimizing the binding of targeted therapeutic drug or imaging agent carriers. There are obvious practical constraints imposed by the body; for example, particles larger than a few microns cannot pass through capillary beds or efficiently enter cells via receptor-mediated endocytosis [1]. Thus, the focus for drug-carrier development is small, nano-scale particles ranging from receptor-conjugated drugs on the order of tens of nanometers to polymer- or lipid-based particles on the order of hundreds of nanometers [2–4]. While specificity of the receptor is a fundamental requirement for disease recognition, optimization of carrier binding is necessary to maximize therapeutic efficacy. This is particularly important when the pathological condition is characterized by a molecular determinant that is normally present at some basal level; thus, one must design the particle to adhere avidly to diseased states but not to quiescent cells which express basal levels of ligand.

Previously we characterized the receptor-mediated adhesion of a 210 nm diameter particle under hydrodynamic flow using a monoclonal antibody as the targeting receptor [5]. In this work, we developed a sensitive assay for the binding of nanoparticles under flow and then used it to establish relationships between adhesion and both receptor density and flow rate. We also established the receptor composition of a particle carrier to maximize adhesion. In this paper, we extend these principles across a wider range of particle sizes relevant for drug delivery.

The effect of carrier size on the rate of adhesion is complex. For instance, the rate of encounter is not a simple function of flow rate because an increase in particle size increases the rate of convective transport and decreases the rate of diffusive transport (the Peclet number increases with particle size). Additionally, the hydrodynamic force exerted by the fluid on the particle scales proportionally with size; thus, detachment is more likely with increasing flow rate. Finally, the contact area increases with particle size, and hence the reaction valency increases. Thus, the overall effect of particle size on adhesion involves numerous competing factors and is, thus, not easily predicted. A complicating issue is that each effect is inherently dependent upon the functional properties of the receptor/ligand binding interaction, such as bond kinetics, mechanics, and length. Therefore, systematic experiments utilizing particles that span the nano-length size scale are required to elucidate these effects.

While there have been systematic investigations of the effect of particle size on adhesion, these studies have focused on the phenomenon

of rolling adhesion using micron-sized particles and did not extend to nanoparticles. Patil and coworkers assessed rolling adhesion of polystyrene beads varying in size from 5 to 20 μm in diameter *via* P-selectin/PSGL-1 interactions and demonstrated that the effective attachment rate was similar at low shear rate but decreased with size at higher shear rates due to increased hydrodynamic drag force [6]. Furthermore, Yago and coworkers investigated tethering of polystyrene beads ranging in size between 1 and 3 μm in diameter *via* L-selectin/PSGL-1 bonding and established that adhesion probability increases proportionately with particle size due to increased encounter frequency, clearly demonstrating a role for slip (or convective) velocity [7]. While these studies are compelling, the micron-scale particles employed are not ideal for *in vivo* targeted delivery, and thus similar studies using nano-scale particles are warranted to quantify the physical mechanisms dominating adhesion. In comparison with microparticles that are primarily affected by shear forces, it is expected that nanoparticle binding will be primarily influenced by diffusion.

Intracellular adhesion molecule (ICAM)-1 is a vascular endothelial cell adhesion molecule that is upregulated during inflammation and has been implicated in leukocyte recruitment *via* activated LFA-1 integrins [8]. ICAM-1 has been linked to pathological settings such as atherosclerosis, autoimmune disorder, transplant rejection, and cancer, and therefore, numerous delivery carriers have been developed to target ICAM-1 [9–11]. However, since ICAM-1 is expressed basally on normal endothelial cells and expressed at higher levels on inflamed endothelium, it represents an excellent model for developing principles to optimize delivery carrier selectivity, as adhesion efficiency must be tuned to insure that normal cells are selectively bypassed in favor of diseased cells. *In vitro* estimates place the ICAM-1 expression at approximately 150 (basal) and 1000 (inflamed) sites/μm^2 [12–14].

Here we examine adhesion of model delivery carriers across the nano-metric length scale using 43 nm and 1.1 μm diameter polystyrene spheres and compare the results with a previous study using 210 nm particles under identical conditions [5]. We utilize a monoclonal antibody specific for ICAM-1 as the targeting receptor and quantify adhesion to ICAM-1 coated glass substrates in a parallel-plate flow chamber at physiological shear rates. Antibody density, ICAM-1 density and shear rate are systematically varied in these experiments to determine quantitatively their effect on particle recruitment and bound state stability. Binding profiles are then analyzed using a transport-reaction model to account for transport phenomena and track particle species, while a Monte Carlo simulation is used to isolate individual particle detachment dynamics from the observed population

behavior. Our results demonstrate that multivalent particle recruitment scales directly with both receptor and ligand densities regardless of size. Furthermore, for a given coating-density of targeting receptor, binding efficiency increases with carrier size. However, fluid flow exerts opposing influences on small and large particles due to a trade-off between the positive influence of receptor/ligand encounter frequency (slip velocity) and the negative influence of shear force, resulting in scenarios under which smaller particles bind more efficiently than larger ones. Surprisingly, once bound to the substrate, particle detachment is independent of size. Using these results in conjunction with our computational tools, we conclude that smaller particles (<200 nm) can be delivered in greater numbers to ICAM-1 expressing cells under the conditions expected *in vivo*. While particles larger than 200 nm bind more efficiently, smaller particles experience higher deposition rates due to enhanced diffusion, and thus, exhibit greater binding selectivity for diseased vessels (higher ICAM-1) relative to normal tissues (normal ICAM-1). Taken together, our findings suggest that a carrier ranging between 100 and 150 nm in diameter would be ideal for targeting ICAM-1 related diseases using the monoclonal antibody that we employed.

MATERIALS AND METHODS

Proteins

Biotinylated anti-human ICAM-1 (clone BBIG, mouse IgG_1 κ) and control (anti-mouse integrin $\alpha_M\beta_2$, rat IgG_{2b}) monoclonal antibodies, ICAM-1/human IgG_1 Fc chimera and control human IgG_1 Fc were purchased from R&D Systems (Minneapolis, MN, USA). Protein G was from Pierce (Rockford, IL, USA). Horseradish peroxidase (HRP)-conjugated rat anti-mouse κ-light chain monoclonal antibody was obtained from Invitrogen (Carlsbad, CA, USA). Mouse anti-human ICAM-1 monoclonal IgG_1 antibody (clone 15.2) was from Ancell (Bayport, MN, USA) and HRP-conjugated rat anti-mouse IgG_1 monoclonal antibody was from BD Biosciences (San Jose, CA, USA). Bovine serum albumin (BSA) was purchased from Sigma (St. Louis, MO, USA).

Particle Functionalization

Neutravidin-coated, yellow-green fluorescent polystyrene Fluospheres (Invitrogen) with diameters of 43 and 1100 nm were functionalized with biotinylated antibody as described previously [5]. For each

sample, 10^{11} (43 nm) or 1.4×10^7 (1.1 μm) particles were diluted in 20 μL Block-Aid (Invitrogen) and sonicated for 5 minutes per manufacturers instructions. This was followed by dilution with PBS containing 1% BSA (PBS^+) and addition of biotinylated antibody (control, anti-ICAM-1, or mixture). Final solution concentrations were 10^{11} (43 nm) or 1.4×10^7 (1.1 μm) particles/mL and 10 μg/mL antibody. The reaction mixture was incubated for at least 1 hour at room temperature on an end-to-end rotator.

Size-exclusion chromatography was used to remove unbound antibody from 43 nm particles. This was carried out using Sephacryl S-500 HR gel filtration media with PBS as the running buffer and an ÄKTA Basic 10 high performance liquid chromatography (HPLC) system (GE Healthcare, Piscataway, NJ, USA). For flow experiments, peak fractions were collected, analyzed for particle concentration using a fluorescence plate reader at 485 nm excitation/527 nm emission, pooled, and diluted with PBS^+ to 10^8/mL concentration. Particle concentration was determined from a calibration curve established from the stock particle solution.

Density gradient ultracentrifugation was used to wash unbound antibody from 1.1 μm particles because they were too large for gel filtration media and pelleting induced aggregation. Density gradients were created in polyallomer ultracentrifuge tubes (Beckman Coulter, Fullerton, CA, USA) using two separate pumps, one distributing OptiPrep (Axis-Shield, Oslo, Norway) density media and the other PBS. The gradients continuously increased from 0 to 12% OptiPrep. After cooling on ice for 15 min, the particle sample was added to the top of the gradient and centrifuged at 40,000 RPM for 30 min at 4°C in an ultracentrifuge. Particles were collected by tube puncture and dialyzed within a 10,000 MWCO Slide-A-Lyzer cassette (Pierce) against 500 mL of PBS three times. Particle concentration was again determined by fluorescence measurement and calibration using the stock particle solution, and samples were diluted with PBS^+ to 5×10^5/mL.

Particle Characterization

Antibody surface density was assessed by enzyme-linked immunosorbant assay (ELISA) using an HRP-conjugated anti-mouse κ-light chain specific monoclonal antibody as described elsewhere [5]. Since this secondary antibody detects the light chains of the antibody, it provides a direct measure of anti-ICAM-1 binding sites. The HRP-conjugated secondary antibody (1:1000 dilution) was added to 1 mL of antibody functionalized particles collected directly from peak

size-exclusion chromatography elution fractions (43 nm) or following density gradient ultracentrifugation and dialysis (1.1 μm), and this solution was incubated at room temperature for 1 h. Samples were then purified using a second round of size-exclusion chromatography or density gradient ultracentrifugation and loaded into an opaque 96-well tissue culture treated polystyrene plate in triplicate to perform the ELISA. Prior to sample addition, 96 well plates were incubated with 0.2 mL StartingBlock (Pierce) per well for 1 hour to prevent deactivation of HRP enzyme by adsorption to the plate walls. Particle fluorescence was first assessed at 485 nm excitation/527 nm emission to determine concentration. Then 50 μL of Amplex Red fluorescent peroxidase substrate (Invitrogen) was added to each well, and after 10 min the Amplex Red signal was measured at 544 nm excitation/590 nm emission. Particle fluorescence signal was negligible using this filter set. Calibration curves were prepared from stock particle and biotinylated HRP (Invitrogen) solutions and used to convert the respective fluorescence intensities to the number of HRP molecules per particle. This was then converted to anti-ICAM-1 binding site density per area of particle (n_r) by assuming a 1:1:1 ratio of binding site to anti-κ light chain antibody to HRP enzyme.

To ensure that 43 nm particles did not aggregate during antibody functionalization, unconjugated control anti-ICAM-1 antibody-coated particles that were collected from the peak size-exclusion chromatography fractions were analyzed using dynamic light scattering (DLS). Particle solutions were mixed in low-volume disposable cuvettes using a pipette, and three runs were performed consisting of 13–15 measurements each on a Zetasizer Nano-S Instrument (Malvern Instruments, Southborough, MA, USA). Particle size distributions were determined by averaging the three runs and calculating the number transformation using the accompanying DTS software (Malvern Instruments).

ICAM-1 Substrate Preparation

ICAM-1 substrates were prepared by attaching ICAM-1/Fc chimera to glass coverslips coated with protein G, as described previously [5]. Briefly, glass coverslips (24 × 50 mm) were cleaned with Piranha solution (66.7% concentrated sulfuric acid and 33.3% hydrogen peroxide), washed extensively with Milli-Q water, dried in a 90°C oven and silanized with 3-aminopropyltrimethoxy silane (Sigma) overnight in an evacuated glass desiccator. Treated coverslips were fitted with modified FlexiPerm (Sigma) silicone gaskets, washed with adsorption buffer (0.1 M $NaHCO_3$, pH 9.2) and incubated for 2 h at room temperature

with a saturating concentration of protein G (100 μg/mL in adsorption buffer). Substrates were then washed three times with PBS to remove excess protein G before addition of Fc protein (Fc control, ICAM-1/Fc or mixture) at 100 nM final concentration. Fc protein mixtures used included 5, 10, and 20% ICAM-1/Fc. Fc protein was incubated for at least 1 h at room temperature before removal immediately prior to use by three rapid washes with SuperBlock (Pierce). The surface density of ICAM-1 (n_l) was characterized by ELISA as previously described [5].

Parallel Plate Flow Chamber Assays

Particle binding experiments were performed using a parallel plate flow chamber with 0.01 inch (0.025 cm) high, 0.35 cm wide rectangular channel as described previously [5]. ICAM-1 coated or control coverslips formed the bottom surface of the flow chamber once assembled, and it was positioned on an inverted Nikon Diaphot microscope equipped with cooled CCD camera, motorized stage and FITC filter cube. Fluorescent images were captured at 40 × magnification with an exposure time of 1 sec for 43 nm particles and 10 × magnification with an exposure time of 500 milliseconds for 1.1 μm particles. The camera and motorized stage were controlled using custom Labview (National Instruments, Austin, TX, USA) programs developed in our laboratory.

Experiments were conducted in two phases, with a particle binding period followed by a detachment period using buffer only. Flow was induced using a syringe pump (Harvard Apparatus, Natick, MA, USA), and the effect of fluid hydrodynamics was investigated using three flow rates that corresponded to wall shear rates of 100, 400, and 1000 s^{-1}. These values are representative of flow within post-capillary venules, large arteries, and arterioles/capillaries, respectively [15]. Wall shear rate $\dot{\gamma}_w$ was calculated from the volumetric flow rate Q as follows

$$\dot{\gamma}_w = \frac{6U}{H} = \frac{6Q}{H^2 W}, \tag{1}$$

where U is the average fluid velocity, H is the chamber height and W is the chamber width. Particle flux was held constant during binding experiments for 1.1 μm particles to maximize particle concentration. Therefore, inlet concentrations used were 5×10^5, 1.25×10^5 and 5×10^4 particles/mL for experiments conducted at 100, 400 and 1000 s^{-1} shear rates, respectively. Particle concentrations used for 43 nm particles were 3×10^7/mL at the 100 and 400 s^{-1} shear rates

and 10^7/mL at 1000 s^{-1} shear rate. A total of eight stage positions near the centerline were monitored for 1.1 μm, starting 5 mm from the inlet and spaced 3 mm apart down the axis. The number of stage positions was decreased to five and the spacing to 1 mm for 43 nm particles to minimize the need to refocus between positions. Complete imaging cycles were completed each minute during the binding period and with decreasing frequency (2–5 min) during the detachment period. Imaging was initiated once particles reached the chamber; however, data were only used after the binding rate reached steady state. This required two min at 100 s^{-1} and one min at the higher shear rates. Binding experiments were conducted for a total of 20 min at 100 s^{-1} shear rate and 14 min at 400 and 1000 s^{-1}. Detachment experiments lasted 30, 15 and 10 min at the same shear rates, respectively.

Binding Profile Analysis

Particle binding isotherms were constructed by manually overlaying consecutive images using a custom Labview program developed in our laboratory. Binding and detachment profiles were constructed by tracking the instantaneous number of particles bound at each time point during binding and detachment experiments, respectively. Attachment profiles were constructed by summing the cumulative number of particles that had bound by each time point during the binding period and therefore, do not reflect detachment. Bound particle numbers were then converted to densities using the known field of view area. Both time and bound particle number were initialized to the beginning of the steady state period, and the results from each of the stage positions were averaged.

Multivalent particle adhesion to the reactive chamber surface is governed by the following rate equation [5]

$$\frac{\partial B}{\partial t} = k_A C_w - \frac{k_D^0}{(t/t_{ref})^{\alpha}} B, \tag{2}$$

where B is the bound particle density, C_w is the unbound particle concentration at the reactive substrate surface, t is time, t_{ref} is a reference time, and k_A and k_D^0 are the multivalent kinetic attachment and detachment rates, respectively. Time appears within the detachment rate in Eq. (2) because dissociation of multivalent particles has previously been shown to vary with time according to a power law denoted by α [5]. The reference time t_{ref} is included simply to preserve consistent unit values between k_D and k_D^0, and was arbitrarily assigned a value of 1 sec. For cases in which α is not known, Eq. (2) must be solved

numerically. However, for attachment data ($k_D^0 = 0$) obtained during the binding phase of experiments, Eq. (2) can be integrated directly as

$$B^{Total} = k_A C_w t, \tag{3}$$

where B^{Total} is the total number of particles bound per area. The attachment rate ($k_A C_w$) is thus given by the slope of B^{Total} plotted *versus* time. Likewise, for detachment experiments ($k_A = 0$), the solution to Eq. (2) is given by

$$B = B_0 \exp\left[\frac{k_D^0}{t_{ref}(1-\alpha)}\left(t_0^{1-\alpha} - t^{1-\alpha}\right)\right], \tag{4}$$

where B_0 and t_0 are the initial bound particle density and time at the start of the detachment period.

Monte Carlo Simulation of Particle Detachment

Multivalent particle detachment is history dependent; therefore, we used a simulation technique to track bound lifetimes for each particle throughout experimental binding and detachment periods and stochastically sample for detachment events, as described elsewhere [5]. In this case the relevant detachment parameters are denoted as κ_D^0 and β to distinguish them from the macroscopic values defined above (k_D^0 and α), and these parameters are used to calculate the detachment probability for each bound particle as follows

$$P_D = 1 - \exp(-\kappa_D \Delta t) = 1 - \exp\left[\frac{-\kappa_D^0}{(t_b/t_{ref})^{\beta}}\Delta t\right], \tag{5}$$

where Δt is the simulation time step and t_b is the total time that the particle has been bound. During each time step, the detachment probability was determined for each bound particle using Eq. (5) and compared with a randomly generated number between 0 and 1. If the random number was less than P_D, the particle was considered to have detached and t_B was recorded. Otherwise t_B was updated by Δt, and the particle remained in the system. Finally, a constant number of newly bound particles was added into the system based on the experimentally determined attachment rate ($k_A C_w$) before proceeding to the next time step. At the conclusion of the simulation, binding profiles were constructed by summing the total number of bound particles at each time step. Detachment experiments were simulated in a similar manner using an attachment rate of zero.

Transport-Reaction Model

The rate constant for particle attachment (k_A) was isolated from the attachment rate ($k_A C_w$) using a transport-reaction model previously described [5]. This enabled tracking of all free and bound particle species throughout the flow chamber, decoupling particle adhesion from effects caused by depletion of particles from the bulk. The model also accounted for convective and diffusive transport, enabling comparison of k_A across different shear rates and particle sizes. The convective-diffusion equation governing particle transport within the flow chamber is given below in dimensionless form, along with the relevant boundary conditions.

$$\frac{\partial \widehat{C}}{\partial \tau} + P\varepsilon[\eta - \eta^2]\frac{\partial \widehat{C}}{\partial \xi} = \varepsilon^2 \frac{\partial^2 \widehat{C}}{\partial \xi^2} + \frac{\partial^2 \widehat{C}}{\partial \eta^2} \tag{6}$$

$$\widehat{C}(\tau, \xi = 0, \eta) = 1 \tag{7a}$$

$$\frac{\partial \widehat{C}}{\partial \xi}(\tau, \xi = 1, \eta) = 0 \tag{7b}$$

$$\frac{\partial \widehat{C}}{\partial \eta}(\tau, \xi, \eta = 1) = 0 \tag{7c}$$

$$\frac{\partial \widehat{C}}{\partial \eta}(\tau, \xi, \eta = 0) = \frac{\partial \widehat{B}}{\partial \tau}(\tau, \xi) = \delta_A \widehat{C}(\tau, \xi, \eta = 0). \tag{7d}$$

The dimensionless variables are defined as follows

$$\begin{array}{llllll} \widehat{C} \equiv \dfrac{C}{C_0} & \widehat{B} \equiv \dfrac{B}{C_0 H} & \xi \equiv \dfrac{x}{L} & \eta \equiv \dfrac{y}{H} & \varepsilon \equiv \dfrac{H}{L} \\ \tau \equiv \dfrac{tD}{H^2} & P \equiv \dfrac{6UH}{D} & \delta_A \equiv \dfrac{k_A H}{D} & & \end{array}, \tag{8}$$

where C is the free particle concentration, C_0 is the inlet concentration, x is the axial coordinate, y is the coordinate perpendicular to the axis, L is the chamber length, D is the particle diffusivity, and U is the average fluid velocity. Particle diffusivity was calculated using the Stokes-Einstein calculation ($D = k_B T/6\pi\mu R_p$, where $k_B T$ is the thermal energy, μ is the fluid viscosity, and R_p is the particle radius). The quantities P and δ_A are the Peclet and Damköhler numbers, respectively. The former relation compares the rates of axial convection with diffusion, while the latter compares the rates of particle binding with diffusive transport. Detachment was not included in

the reactive boundary condition (Eq. (7d)) due to the dependence on time, as a time-dependent detachment rate would make solution of the model intractable. Therefore the model was used to fit attachment data ($k_D^0 = 0$) exclusively. Particle motion lateral to the direction of flow was omitted despite the fact that the gravitational force vector is oriented toward the bottom surface of the chamber because particle sedimentation estimates indicate that gravity should have a negligible effect on binding. For instance, the 1.1 μm particles will sediment less than one particle radius over the 26 mm of flow chamber surface monitored at 100 s^{-1} shear rate. Furthermore, the rate of sedimentation is 200-fold lower than the rate of diffusion. Scaling comparisons for the rates of convection, diffusion and sedimentation are listed in the supporting information.

Finite-element solution of the model was performed using Comsol Multiphysics software employing the two-dimensional transient convection-diffusion application to account for bulk transport within the flow chamber and the weak form boundary application to incorporate the reaction at the adhesive boundary. Solutions utilized a 1 sec time-step and were carried out for a total of 14 or 20 min to emulate binding experiments. Binding phenomena were tracked at discrete nodes placed at points that correspond to the axial positions observed during experiments, and k_A was determined by averaging the bound particle densities at each node and matching with the observed attachment rate. The dimensional parameters used to calculate the dimensionless parameters in Eq. 8 are reported in the supporting information.

Statistics

ELISA results and bound particle densities are given ± the standard error for at least three independent experiments. Curve fitting results used in determination of the attachment rate ($k_A C_w$) and attachment rate constant (k_A) are given ± the standard error of the data. All other curve fits are given ± 95% confidence interval.

RESULTS

Characterization of Molecular Densities

Anti-ICAM-1 binding site density (n_r) was determined for 43 nm and 1.1 μm particles by ELISA (Fig. 1A). 43 nm particles were incubated with biotinylated anti-ICAM-1 antibody at 5, 25, and 100% mass ratios with a biotinylated control antibody, resulting in anti-ICAM-1 binding site densities of 1600 ± 220, 3030 ± 280 and 4980 ± 460 μm^{-2}. Similar

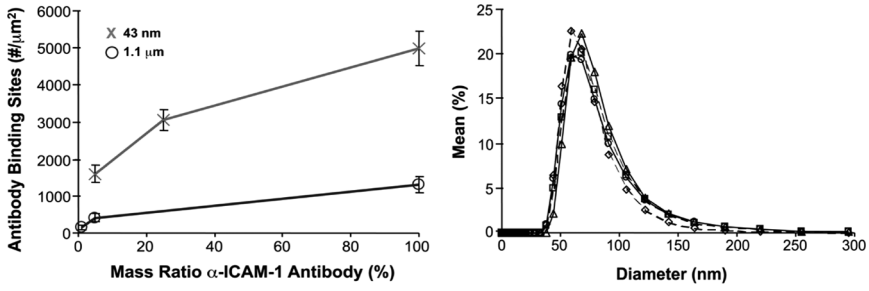

FIGURE 1 Characterization of polystyrene model delivery carriers. (A) Anti-ICAM-1 binding site density was measured for 43 nm and 1.1 μm particles by immuno-ELISA using HRP-conjugated rat anti-mouse κ-light chain specific monoclonal antibody. For 43 nm particles, Neutravidin-coated particles were incubated with 10 μg/mL total biotinylated antibody at 5, 25 and 100% ratios of anti-ICAM-1 antibody with control antibody. Coating conditions were similar for 1.1 μm particles except incubation ratios were 1, 5 and 100%. (B) Size distribution of 43 nm particles measured by dynamic light scattering demonstrating mono-modal nature of unconjugated particles (dashed lines) and particles conjugated with anti-ICAM-1 antibody (solid lines). Two samples of each species are represented, corresponding to separate size-exclusion chromatography fractions. Error bars represent the standard error of at least three independent measurements.

treatment of 1.1 μm particles at 1, 5 and 10% ratios of anti-ICAM-1 antibody yielded densities of 150 ± 70, 410 ± 110 and $1310 \pm 230\,\mu m^{-2}$. These densities correspond to approximately 9, 18, and 29 binding sites per 43 nm particle and 600, 1580 and 4970 per 1.1 μm particle.

ICAM-1 substrates were prepared by linking an ICAM-1/Fc chimera to protein G coated glass coverslips. ICAM-1 site density (n_l) was modulated using a control Fc protein, and the conjugation conditions employed here were identical to a previous study [5], which were measured by ELISA to be 21 ± 1, 41 ± 3 and $134 \pm 6\,\mu m^{-2}$. This study also utilized an additional surface prepared from a 20% molar ratio of ICAM-1/Fc with the Fc control, which yielded an ICAM-1 density of $82 \pm 4\,\mu m^{-2}$.

Dynamic Light Scattering of 43 Nm Particles

Unconjugated control and anti-ICAM-1 antibody conjugated 43 nm particles were analyzed by DLS to determine the size distribution before and after antibody functionalization and confirm that the

particles were not aggregating. For both cases, samples were obtained from the peak size-exclusion chromatography elution fractions. The results using number transformation are given in Fig. 1B and show that the size distribution in each case is monomodal with an average peak at 70 nm and a width of 30 nm. This confirms that the particles are uniformly sized with negligible aggregation or cross-linking. The average size is considerably larger than that specified by the manufacturer, which may have been measured for polystyrene particles prior to processing and Neutravidin coating. We will report our results based on the advertised polystyrene particle size.

Particle Binding and Detachment

Binding and detachment profiles from flow chamber experiments are shown in Fig. 2 for both 43 nm (A–C) and 1.1 μm (D–F) particles. Each trace represents different particle receptor or substrate ligand density conditions, while each panel of the figure represents different shear rates. Since inlet particle concentrations and total experiment times varied between each plot, final particle densities cannot be compared directly. Nonspecific adhesion levels were determined for control particles and substrates. This adhesion was then subtracted from the raw adhesion data before plotting Fig. 2. Generally nonspecific adhesion increased with shear rate (due to greater particle flux) and decreased with particle size (data not shown). Detachment experiments followed binding experiments after particles were washed from the chamber using a buffer solution and involved monitoring the decrease in bound particles with time. Particle detachment was observed for all particle sizes at low shear rates; however, at elevated shear rates detachment was only observed for 43 nm particles on high ICAM-1 densities.

Determination of Attachment Rate from Binding Experiments

Particle attachment profiles were constructed by tracking the total number of particles bound during binding experiments. The attachment rate $k_A C_w$ was then obtained from the slope of the attachment profiles by linear least-squares regression using Eq. (3). After normalization by inlet concentration, the attachment rate ($k_A C_w/C_0$) was then plotted *versus* the product of receptor and ligand density, $n_r n_l$, for both 43 nm (Fig. 3A) and 1.1 μm (Fig. 3B) particles. This replotting illustrates the linear relationship between attachment rate ($k_A C_w/C_0$) and $n_r n_l$, confirming similar results from previous studies using both nano- and micron-scale particles [5,7]. Adhesion rates for

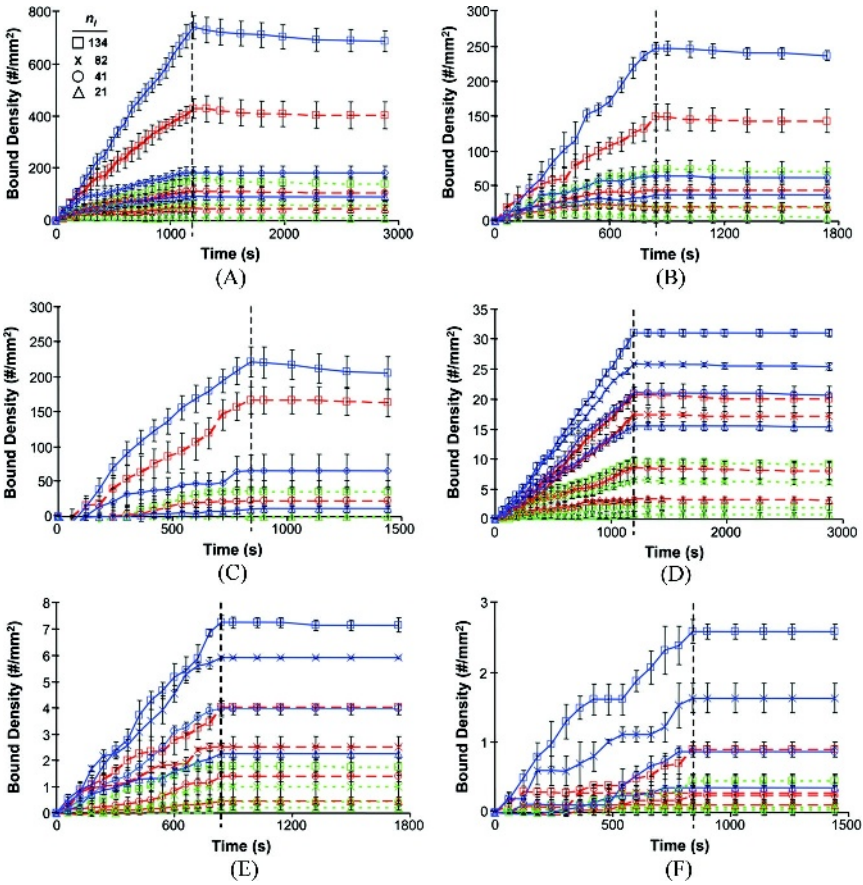

FIGURE 2 Binding profiles for (A–C) 43 nm and (D–F) 1.1 μm particles in flow chamber assays at (A, D) 100, (B, E) 400 and (C, F) 1000 s^{-1} shear rates. Colors designate low (green), medium (red), and high (blue) antibody density (n_r) particle conditions (see particle characterization results section) and shapes correlate to different ICAM-1 substrate densities (n_l) as indicated by the legend. The vertical dashed lines designate the transition between binding and detachment experiments. Error bars represent the standard error of at least three independent binding experiments.

1.1 μm particles were substantially greater than observed for 43 nm particles. The rate of 1.1 μm particle binding at the lower shear rates saturated at high attachment rate, which was likely caused by depletion of particles from the region near the reactive wall. Saturation was not observed for 1.1 μm particles at a shear rate of 1000 s^{-1} or for

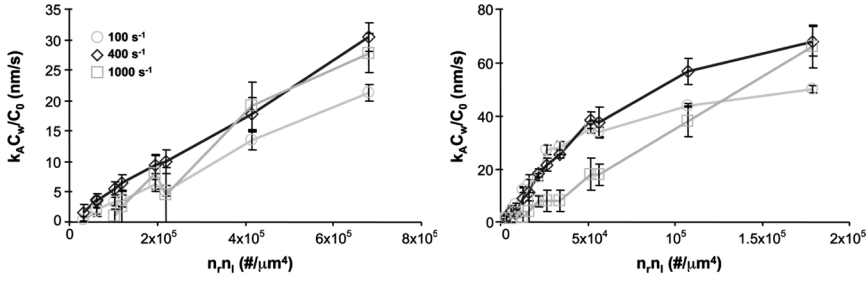

FIGURE 3 Observed particle attachment rate ($k_A C_w/C_0$) for (A) 43 nm and (B) 1.1 μm particles obtained by fitting the cumulative particle binding profiles ($k_D = 0$) from binding experiments using Eq. (3). Results indicate that the larger particles bind more efficiently than the 43 nm particles. In addition, 1.1 μm particle binding appears to saturate at high receptor and ligand densities for the lower shear rates, suggesting that particle depletion is significant at these conditions. Error bars indicate the standard error of at least three independent experiments.

43 nm particles. Figure 3 also suggests that shear rate influences attachment rate.

Evaluation of Detachment Rate Parameters from Detachment Experiments

To determine the macroscopic detachment dynamics of the 43 nm and 1.1 μm particles, detachment experiment profiles were simultaneously fit to both k_D^0 and α parameters using Eq. (4). This resulted in best-fit α values ranging from 0.2 to 0.6 (average 0.4 ± 0.15) for 43 nm particles and 0.1 to 0.7 (average 0.28 ± 0.19) for 1.1 μm particles. The average values for α are very close to the value of $\frac{1}{3}$ previously determined for 210 nm particles using the same antibody-antigen chemistry [5]. This led us to conclude that α, the functional time-scale dictating the rate at which particle detachment rate decreases with time, does not vary appreciably with particle size. Therefore single-parameter (k_D^0) fits were performed holding α at $\frac{1}{3}$, and the results are shown for representative samples in Fig. 4 (all values listed in the supporting information).

In our previous study using 210 nm particles, an inverse correlation was established between k_D^0 and both n_r and n_l [5]. However, the scaling relationships were not the same, with k_D^0 varying directly with n_r ($1/\sqrt{n_r}$) and indirectly with n_l ($1/n_l^{1/3}$). Correspondingly, we plotted the values of k_D^0 obtained for 43 nm and 1.1 μm particles as a function

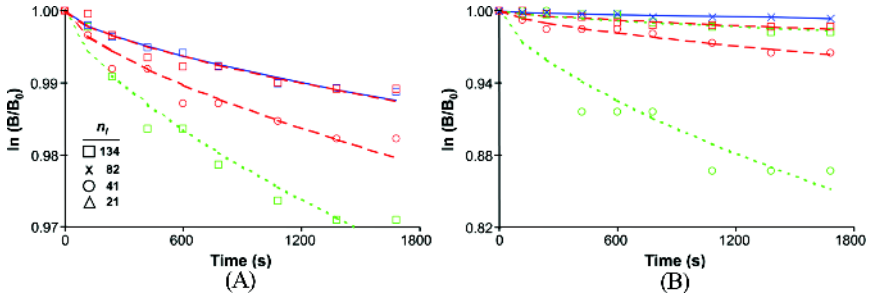

FIGURE 4 Detachment experiment profile fits obtained using Eq. (4). The data is presented as the natural logarithm of the bound density, normalized to the initial value at the start of the detachment period (B_0). Results shown include representative examples for both (A) 43 nm and (B) 1.1 μm particles at different adhesion molecule density conditions and 100 s^{-1} shear rate. For all cases, fits were obtained for $\alpha = \frac{1}{3}$ regardless of particle size. Colors again designate low (green), medium (red), and high (blue) antibody density particles (see particle characterization results section) and shapes correlate to different ICAM-1 density substrates as indicated by the legend.

of $1/(n_r n_l^{\phi})$, where ϕ is an unknown constant that accounts for the non-linear influence of ligand density. Evaluation of these fits led us to conclude that k_D^0 did indeed vary inversely with n_r for both 43 nm and 1.1 μm particles, while the relationships with n_l were best represented by ϕ values of 1/5 and 1, respectively. These relationships are illustrated in Fig. 5 using the data obtained at 100 s^{-1} shear rate. Taking into account the ϕ value of $\frac{1}{3}$ observed for 210 nm particles, it is clear that the scaling relationship between detachment rate and ligand density depends on particle size, with ligand density exerting greater influence as size increases. Interestingly, despite different values of ϕ, the slopes obtained from plotting k_D^0 *versus* $1/(n_r n_l^{\phi})$ did not vary substantially with particle size (3.4 ± 0.5, 4.2 ± 0.4 and 3.8 ± 0.6 for 43 nm, 210 nm and 1.1 μm particles, respectively), suggesting that this relationship may represent a fundamental property of particle detachment with ϕ accounting for the net influence of particle size. Plotting ϕ *versus* particle radius yielded a straight line with slope equal to $1.5 \pm 0.2\,\mu m^{-1}$ and intercept of 0.17 ± 0.05 (Fig. 5C). Using this result, k_D^0 was then plotted in Fig. 5D for each particle size using the 100 s^{-1} shear rate data, which yielded an excellent linear fit with a generalized slope of 3.9 ± 0.2. The k_D^0 values observed for 43 nm particles at elevated shear rates did not vary significantly from lower shear rates, which was expected because k_D^0 has already been shown to be insensitive to shear rate for larger 210 nm particles [5].

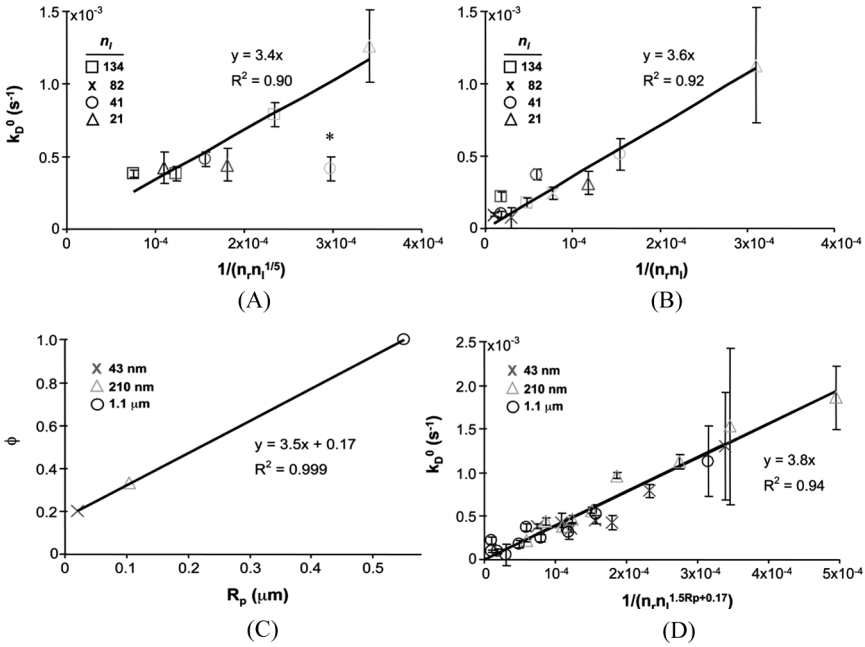

FIGURE 5 Appropriate scaling of the detachment rate constant (k_D^0) to the receptor and ligand densities reveals consistent behavior across different particle sizes. (A and B) Plots of k_D^0 versus $1/(n_r n_l^{\phi})$ for (A) 43 nm and (B) 1.1 μm particles at 100 s^{-1} shear rate to demonstrate that the data is most accurately represented using ϕ values of 1/5 and 1, respectively. The data point indicated by $*$ was not used for fitting purposes. In a previous study, ϕ was determined to be $\frac{1}{3}$ for 210 nm particles under identical conditions [5]. (C) Plotting ϕ versus particle radius (R_p) suggests that this relationship is linear, and plotting the detachment data for all particles together against the generalized equation $1/(n_r n_l^{1.5Rp+0.17})$ resulted in a good fit for all three particle sizes. The shapes in the figure correlate to different ligand density conditions as indicated by the legend. Error bars indicate 95% confidence intervals for regression analysis fits.

Stochastic Simulation of Detachment

Detachment simulations were performed using Matlab to establish self-consistent rate parameters (κ_D^0 and β) that are simultaneously applicable to both binding and detachment experiments, which is not the case for the time-averaged values (k_D^0 and α) determined above. Simulations were conducted using Matlab with a time step of 1 sec, and for each condition three independent simulations were averaged to aid data fitting. During each time step, particles were introduced

into the system based on the attachment rate ($k_A C_w$) established from binding experiments, and detachment was then stochastically sampled based on the detachment probability defined by Eq. (5). The detachment parameters (κ_D^0 and β) were then chosen to fit binding and detachment experiment data simultaneously. After inspection, the best-fit value for β across all experimental conditions was $\frac{3}{4}$. This is the same β value determined for 210 nm particles previously, as expected due to similarity in α values established above [5]. Using $\beta = \frac{3}{4}$, κ_D^0 was then selected to match the binding and detachment experiment profiles. In some cases, successful matching of the binding experiment data required increasing the attachment rate. This correction has been shown to account for a subpopulation of particles that remain bound for only seconds to tens of seconds before detaching [5], which would be missed due to the exigencies of gathering binding data rapidly. Calculated profiles for binding and detachment for 43 nm and 1.1 μm particles at 100 s^{-1} shear rate are presented in Fig. 6. Values determined for κ_D^0 are listed in the supporting information.

Based on the scaling relationships established for adhesion molecule density and particle size in the previous section and these

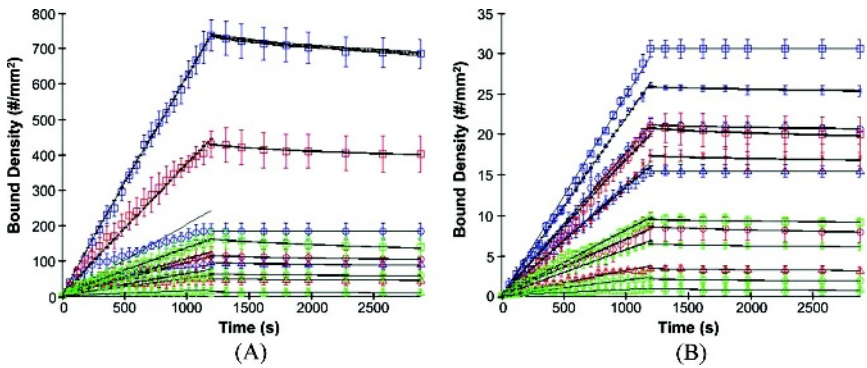

FIGURE 6 Stochastic simulation fits of binding and detachment experiment data for (A) 43 nm and (B) 1.1 μm particles at 100 s^{-1} shear rate that were obtained using the self-consistent, time-dependent power law scaling relationship defined by Eq. (5). The parameter β, which determines the time scale over which adhesion strengthening occurs for the multivalent particles while bound, was equal to $\frac{3}{4}$ for all particle size, shear rate and molecular density conditions tested. Colors and symbols represent the same receptor and ligand densities as in Fig. 2. Error bars indicate SE for binding and detachment data and SD between three independent simulations for stochastic fits.

simulations, a self-consistent dissociation rate constant can be defined as follows

$$\kappa_D = \frac{\kappa_D'^0}{n_r n_l^{(1.5R_p+0.17)}(t_b/t_{ref})^{3/4}}, \tag{9}$$

where the constant $\kappa_D'^0$ is approximately equal to 87 but will undoubtedly be dependent on the kinetic rates ($k_f = 1.6 \times 10^5\,\mathrm{M^{-1}s^{-1}}$, $k_r = 1.1 \times 10^{-4}\,\mathrm{s^{-1}}$ [16]) and the mechanical and structural properties of the antibody/ICAM-1 interaction. Therefore, it is unique to this chemical system. The relationship between n_l and particle size is also likely to be influenced by receptor/ligand properties.

Determination of k_A From Attachment Data

The attachment rate constant (k_A) was isolated from the attachment rate ($k_A C_w$) using a finite-element software package (Comsol Multiphysics) to solve Eq. (6) subject to boundary conditions 7a–d. Model solutions were obtained by manually iterating the parameter δ_A (non-dimensionalized form of k_A) to match the simulated adhesion rate to the experimental attachment rate, adjusted based on the stochastic simulations if necessary ($k_A C_w^{Total}$). k_A was then determined by re-dimensionalizing δ_A, and all values are listed in the supporting information. Plotting k_A versus $n_r n_l$ resulted in linear relationships for both 43 nm (Fig. 7A) and 1.1 μm particles (Fig. 7B). Slope values determined by linear regression were 3.5 ± 0.2, 4.8 ± 0.1 and 5.8 ± 0.8 nm/s for 43 nm particles at 100, 400 and 1000 $\mathrm{s^{-1}}$ shear rates, respectively. Comparative values for 1.1 mm particles were 152.5 ± 4.9, 119.3 ± 5.4 and 49.1 ± 4.7. The intercept for the fit of the 43 nm particles at 1000 $\mathrm{s^{-1}}$ shear rate was non-zero, but this datum was error-prone due to a large noise to signal ratio. Comparison of Figs. 7A and B suggests that fluid flow has opposing effects on particle recruitment for the two particle sizes. For the 43 nm case, increasing fluid flow rate increases the adhesion rate, while for 1.1 μm particles increasing fluid flow decreases the adhesion rate. For 210 nm particles, adhesion rate increased with shear rate as was seen with 43 nm particles [5]. This suggests that at some particle size between 210 nm and 1.1 μm, the negative influence of particle size on detachment (shear force) outweighs the positive contributions of particle size on binding efficiency (convective transport and contact area).

To quantify the dependence of attachment rate on flow, the slopes from k_A versus $n_r n_l$ curves were plotted against shear rate in Fig. 7C. The results obtained previously for 210 nm particles were also included

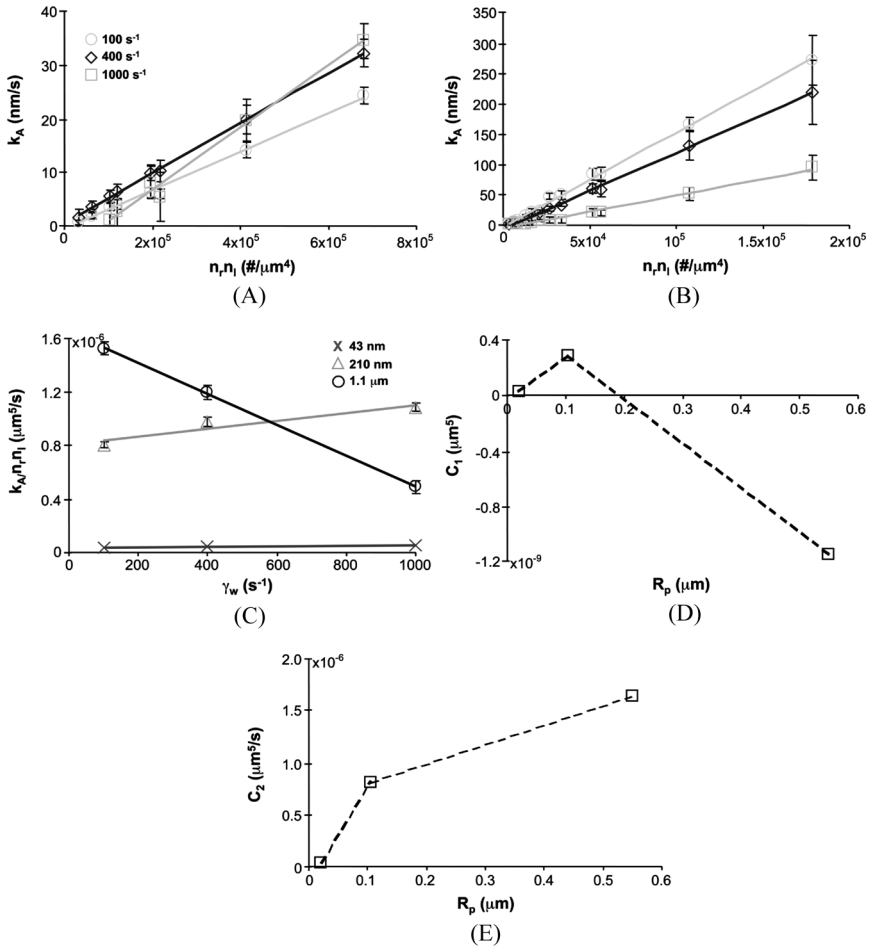

FIGURE 7 Attachment rate constant (k_A) scaling with adhesion molecule density, shear rate, and particle size. After isolation of k_A using the transport-reaction model, the results for (A) 43 nm and (B) 1.1 μm particles were plotted against $n_r n_l$ to remove the influence of the adhesion molecule densities. This relationship was linear for all cases even out to the highest attachment rates, indicating that the attachment rate saturation effects observed for 1.1 μm particles in Fig. 2 is caused by depletion of particles from the region near the reactive wall. (C) The dependence of k_A on shear rate was investigated by plotting the slope of the k_A versus $n_r n_l$ plots from A and B against shear rate. The results using 210 nm particles from a previous study are included as well [5]. Binding efficiency increases with particle size at low shear rate; however, shear increases attachment rate for 43 and 210 nm but decreases binding efficiency for 1.1 μm particles. Linear fits were then

for comparison [5]. For each case, the response to shear rate was apparently linear. We expect that particle attachment will depend on the product of shear rate and particle size, $\dot{\gamma}_w R_p$, or slip velocity [17]. Thus, a linear relationship between flow rate and attachment is reasonable. In contrast, detachment should scale with $\dot{\gamma}_w R_p^2$ based on the Stokes equation for drag force [7]. Since both slip velocity and shear force vanish when shear rate is zero, one will dominate from the onset of flow. With a linear relationship established, attachment rate can thus be characterized by two constants that dictate the contribution from shear rate dependent (slope, C_1) and independent (intercept, C_2) factors. Linear regression resulted in C_1 values of 2.5, 28.7 and −114.6 for 43, 210 and 1100 nm particles, respectively. Corresponding C_2 values were 3.5, 81.0 and 164.0 for 43, 210 and 1100 nm particles, respectively. Interestingly, 1.1 μm particle adhesion was most efficient at low and intermediate shear rates, but 210 nm particles adhesion was greatest at the highest shear rate. By interpolation, binding efficiency for the 210 nm and 1.1 μm particles should be equivalent at approximately 600 s^{-1} shear rate. The binding efficiency of 43 nm particles was considerably lower than the other sized particles and remained relatively unaffected by shear rate. It should be noted that these findings do not reflect the contribution of diffusion, which is removed by the transport-reaction model.

The fitting constants C_1 and C_2 vary with particle size and therefore can be used to reveal the role of size in recruiting particles. Plotting C_1, which dictates the magnitude of shear-rate dependent effects, *versus* R_p resulted in a biphasic curve, rising initially between 43 and 210 nm particles and falling to 1.1 μm (Fig. 7D). Hence the relationship between C_1 and particle size would best be characterized by a second order polynomial with negative second order and positive first order terms, which follows the expected particle scaling for the effect of particle size on hydrodynamic shear force and convective

performed to yield unique constants that capture the shear-rate dependent (slope, C_1) and shear-rate independent (intercept, C_2) factors. (D) Plotting C_1 against particle size resulted in a biphasic curve that appears to follow second-order polynomial functionality with negative quadratic, positive linear and seemingly negligible constant terms. These results correlate with the expected scaling relationships and relative influence of hydrodynamic shear force, slip velocity and encounter duration, respectively. (E) C_2 increases with particle size but appears to approach saturation at micron diameters. Error bars for k_A represent the data SE from attachment rate fits that were propagated through the transport-reaction model. Error bars for $k_A/n_{,}n_l$ indicate 95% confidence intervals for linear regression fits.

velocity, respectively. These factors appear to be balanced ($C_1 = 0$) for a particle size between approximately 600 and 800 nm diameter, which would make adhesion efficiency independent of shear rate. The constant term appears to be negligible and likely correlates to the influence of encounter duration. The response of C_2, which gauges the influence of shear-rate independent parameters such as contact area size and the chemical, mechanical and structural properties of the receptor/ligand interaction, increased with particle size until saturation at 1.1 μm (Fig. 7E). In summation, use of larger particles is advantageous to maximize shear-rate independent adhesion (C_2); however, consideration must also be given to the local flow conditions at the target site to maximize shear-rate dependent factors (C_1).

DISCUSSION

In this paper we explored the effect of particle size on scaling laws for attachment and detachment of particles ranging from 43 to 1,100 nm in diameter, using an identical antibody/antigen system. We extended methods developed previously for the binding of 210 nm particles [18] to explore the effects of particle size on adhesion.

Evaluation of particle detachment revealed that the canonical functional form for particle detachment was conserved over a wide spectrum of adhesion molecule density, shear rate and particle size. All particle sizes illustrate a shared dependence of detachment rate on bound time, but the detachment rate also illustrates consistent power law scaling (fundamental $\beta = \frac{3}{4}$) with the effect of time. The detachment rate of a multivalent particle would be expected to decrease with increasing time since adhesion can strengthen during contact between a particle and surface regardless of particle size. Since bond number must ultimately govern detachment dynamics, the factors that control bond formation, such as chemical or structural properties of the receptor/ligand interaction, are likely to affect adhesion strengthening (*i.e.*, β). It remains to be seen how values of β will depend on receptor size and density as illustrated by other receptor/ligand pairs displaying different kinetic, mechanical and structural characteristics.

Previously we determined that the detachment rate (k_D^0 or κ_D^0) for 210 nm particles scaled with adhesion molecule density when normalized to $1/(n_r n_l^{\phi})$, where ϕ was approximately $\frac{1}{3}$ [5]. Similar results were obtained here for 43 nm particles, except the best fit was obtained for $\phi = 1/5$. Conversely, detachment was only observed at the lowest shear rate for 1.1 μm particles, and within this data set, the detachment rate scaled directly with n_l ($\phi = 1$). Interestingly, for each particle size the slope of detachment rate plotted as a function of $1/(n_r n_l^{\phi})$ was

approximately equal. Consequently it appears that an inverse relationship with n_r is a fundamental property of particle detachment, while the influence of n_l on detachment rate diminishes with particle size. Plotting ϕ *versus* R_p indicated that the effect of n_l is directly proportional to particle size. While the fundamental basis for ϕ is not known at this time, its behavior scales with the predicted difference in available surface area within the contact zone between the spherical cap of the particle ($SA_C = 2\pi R_P L_C$) and the projected area of the particle onto the underlying substrate ($PA_C = SA_C - \pi L_C^2$). Here L_C refers to a characteristic length that is on the order of the bond length (typically the bond length subtracted by the minimum separation distance between the particle and substrate). Applying an estimate for L_C in this antibody/ICAM-1/Fc system of 15 nm, the ratio PA_c/SA_c is 0.65, 0.93, and 0.99 for 43, 210, and 1100 nm particles, respectively. We suggest that the monotonic relationship between ϕ (0.2, 0.33, and 1) and the ratio PA_c/SA_c indicates a fundamental relationship that may inform the role of particle size and molecular size on adhesion. Thus, it appears that ϕ reflects the state of the contact zone and the length-scale of the receptor/ligand bond, where the relatively high degree of particle curvature associated with small particles diminishes the significance of ligand density. In contrast, the relatively planar geometry seen with large particles renders the contributions from both receptor and ligand equivalent. Our results also imply that ϕ would not continue to increase for particles larger than a micron in diameter, since this value appears to be saturating at 1. Additional insight into the origin of ϕ, as with the power law β that governs adhesion strengthening, will require further experiments using different receptor/ligand systems or the use of adhesive dynamics simulations that assess particle bonding interactions with the appropriate molecular detail [19,20]. It should be noted that the detachment rate itself should eventually reach a limit at low receptor or ligand densities, when there is only a single tether in the contact zone.

Shear rate did not significantly influence the detachment rate of particles smaller than 210 nm. However, it did bring about the paradoxical outcome for micron-sized particles in which detachment was observed at low shear rate but not at the higher values. The maximum tether force experienced by a bound particle ($F_t^{Max} = 13.2\mu\dot{\gamma}_w R_p^2$, [21,22]) is predicted to be less than 1 pN for 43 and 210 nm particles at the shear rates investigated, as well as for 1.1 μm particles at 100 s^{-1} shear rate. The strength of a single antibody/antigen bond, on the other hand, has been shown in numerous studies to be greater than 10 pN [23]. Therefore, it is reasonable to conclude that hydrodynamic force plays a negligible role in particle detachment at these conditions. In this limit,

particle detachment would be independent of mechanics and, thus, dominated by the kinetics of bond formation and breakage. Conversely, F_t^{Max} is greater than 1 pN for 1.1 μm particles at 400 and 1000 s^{-1} shear rates (1.6 and 5, respectively) and, thus, the shear force could be on the same order of magnitude as the bond strength. The absence of detachment at these conditions suggests that the influence of shear flow is exerted during binding, as particle arrest should occur only if the initial attachment event is capable of withstanding the shear force. Hence, a bias may exist at elevated shear forces towards higher initial bond numbers, decreasing the likelihood of detachment. Requirement of multiple bonding for initial particle arrest would also decrease adhesion rate, as observed in this study for the binding of 1.1 μm particles at higher shear rates. Brownian motion of a tethered particle will also generate forces and torques that could contribute to bond disruption. This contribution is not expected to be significant for 1.1 μm, as adhesive dynamics simulations of red blood cells tethered to a surface by a single bond have indicated that bond disruption forces arising from Brownian motion are on the order of 0.005 pN and, thus, negligible [18]. Bond disruption forces caused by diffusion of nanoparticles have not been studied and are expected to be insignificant.

Attachment of 43 nm and 1.1 μm particles scaled directly with both receptor and ligand densities, or $n_r n_l$, as demonstrated previously for nano- and micron-scale particles [5,7]. Using the dependence of k_A on $n_r n_l$, we could independently assess the impact of flow rate on particle attachment. Plotting $k_A/n_r n_l$ *versus* shear rate for 43, 210 and 1100 nm particles resulted in an apparently linear relationship between hydrodynamic flow and particle attachment for each case (Fig. 7C). However, the net effect of shear rate differed considerably for nano- and micron-scale particles, as increasing shear rate increased adhesion rate for the 43 and 210 nm cases but decreased adhesion for 1.1 μm particles. Competing factors are clearly at play and, based on the expected linear scaling, we concluded that these factors were particle slip velocity and hydrodynamic shear force, which scale with $\dot{\gamma}_w R_p$ and $\dot{\gamma}_w R_p^2$, respectively [7,17,21]. Shear force, thus, becomes the dominant factor for particles greater than 210 nm, requiring greater initial bond numbers to successfully tether the larger particles from flow. To elucidate further the effect of particle size, the flow-dependent (slope, C_1) and flow-independent (intercept, C_2) components from the attachment rate *versus* shear rate plots were isolated by linear regression. Plotting C_1 *versus* particle radius yielded a curve with apparent second order polynomial functionality, including negative second order, positive first order and negligible constant terms. This scaling correlates precisely with the mathematical dependence of hydrodynamic shear

force and slip velocity on particle size. Based on shape of the curve, slip velocity dominates adhesion for smaller nanoparticles before being overtaken by shear force, and it appears that the factors are balanced for a particle approximately 600 to 800 nm in diameter. The constant term is likely related to contact duration, which is given by the inverse of the shear rate. Thus, we conclude that the forward reaction rate for the antibody/ICAM-1 interaction ($k_f = 1.6 \times 10^5\,\mathrm{M^{-1}s^{-1}}$, [16]) used here is sufficiently fast to render this constant term insignificant. The factor C_2 increased nonlinearly with size, saturating at a diameter of 1.1 μm. Hence larger particles fundamentally bind with greater efficiency, per adhesion molecule, which is likely due to the larger contact area size. Additional experiments with different receptor ligand systems and simulations will be required to specify fully the functional form for C_1 and C_2 with respect to particle size.

Based on the attachment rates measured, it would appear that a specific particle size is optimal for targeting different areas of the vasculature depending on the local hydrodynamic flow environment. Properly accounting for transport limitations within a specific local flow environment is of particular importance for designing delivery carriers that target molecular determinants that are also expressed at a basal level on normal tissues. To illustrate how these factors translate within the context of ICAM-1 targeting on inflamed endothelium, we calculated the expected particle delivery potentials at both normal and inflamed ICAM-1 expression densities. This was accomplished by calculating k_A (slope values from k_A *versus* $n_r n_l$ plots at $100\,\mathrm{s^{-1}}$ shear rate) and κ_D^0 (Eq. (9)) for 43, 210 and 1100 nm particles at the ICAM-1 expression levels reported for normal ($n_l^N = 150/\mu\mathrm{m}^2$) and inflamed ($n_l^D = 1000/\mu\mathrm{m}^2$) endothelial cells *in vitro*, over the range of particle receptor densities that we could attain experimentally. The transport-reaction model (Eqs. (6)–(7a–d)) was then used to determine the observed attachment rate over an arbitrarily chosen 10 cm long section of reactive ICAM-1 surface for 10 min based on a bulk particle concentration of 10^7/mL. Finally, particle detachment was assessed using the stochastic simulation based on the observed attachment rate, calculated κ_D^0 value and $\beta = \frac{3}{4}$, both during the 10 min binding period as well as the ensuing 10 min. Due to evidence from our previous study that detachment rate does not decrease indefinitely, κ_D^0 was not allowed to exceed $0.05\,\mathrm{s^{-1}}$ [5]. The ratio of particle densities delivered to the diseased and normal cases (B^D/B^N) are plotted *versus* n_r in Fig. 8A for each particle size studied. These results indicate that particle depletion effects lead to decreased selectivity as binding rate increases, and this effect is more pronounced for larger particles. This is a direct consequence of smaller

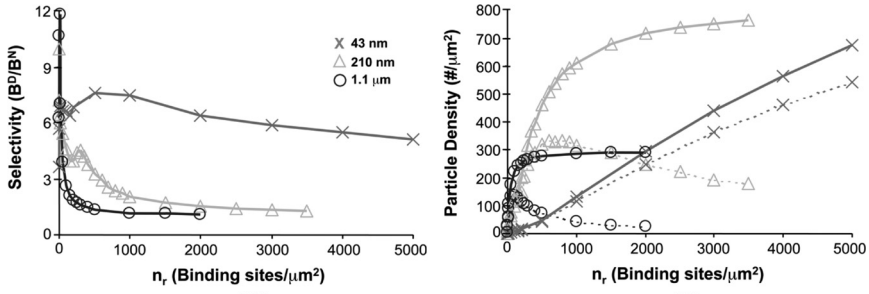

(A) (B)

FIGURE 8 Simulated calculation of carrier delivery to endothelial ICAM-1 expressed at normal ($n_l^N = 150/\mu m^2$) and inflamed ($n_l^D = 150/\mu m^2$) densities. Attachment rate was determined for 43, 210 and 1100 nm diameter particles at each ligand density based on experimental results at 100 s^{-1} shear rate, and the transport-reaction model was used to determine the resulting attachment rate. Specifically, transport-reaction model solutions were obtained assuming exposure of a 10-cm long section of blood vessel to a bulk concentration of 10^7 carriers/mL for 10 min. The attachment rate was then used along with the appropriate κ_D^0 value (Eq. (9)) and $\beta = \frac{3}{4}$ in the stochastic detachment simulation to assess particle dissociation during the binding period and for a 10 min period afterwards. (A) Selectivity, defined as the ratio of particles delivered to the diseased and normal cases (B^D/B^N), decays for all particles as receptor density increases due to increasingly higher binding rates at normal ligand density. However, selectivity remains greater at higher receptor densities for smaller particles. The decay in selectivity is discontinuous for 43 or 210 nm particles, as local maxima are observed due to the non-linear relationship between κ_D^0 and n_l (ϕ less than 1). (B) Total delivery density for the diseased case (B^D, solid lines) and the difference between the diseased and normal cases ($B^D - B^N$, dotted lines) plotted against particle receptor density. Delivery potential saturates quickly for the larger particles, and at lower delivery levels, as a result of rapid depletion of particle concentration near the vessel wall. Saturation was not observed for the 43 nm particle size because receptor-coating density was limiting. Thus smaller particles can be delivered at higher levels despite lower intrinsic attachment rate (see Fig. 7). Based on the combined factors of adhesion efficiency, depletion effects and receptor coating limitations, the ideal particle size would be 100–150 nm in diameter for this targeted delivery application.

particles having a higher rate of diffusion and, thus, a greater capacity to overcome particle depletion from the near-wall region. As Fig. 8B demonstrates, decreasing particle size not only leads to increased selectivity, but can also increase the yield, or rate, of particle binding to diseased tissues. This change occurs because the elevated diffusion rate compensates for the decreased binding rate. The combined

influence of selectivity and total delivery potential is also exhibited in Fig. 8B by the difference between binding to the diseased and normal cases ($B^D - B^N$), which again demonstrates that targeting selectivity is greatest for smaller particles. Figure 8B also suggests that the 43 nm particles were unable to attain their maximum binding potential, on account of the physical limitations of antibody-coating density. Thus, the ideal carrier would be one that is small enough to exhibit high selectivity but large enough to attain the maximum theoretical delivery potential, which for this application would be obtained for a carrier between 100 and 150 nm diameter.

The findings described in this work regarding particle size and targeting receptor density optimization are unique to the case at hand, namely the particle adhesion rate observed for the BBIG anti-ICAM-1 antibody and the reported ICAM-1 expression levels on endothelium. If the target expression density were considerably lower, for instance on the order of hundreds rather than thousands of sites/μm^2, then the ideal particle size would increase. Likewise, if a targeting receptor were used that displayed lower binding efficiency, a larger particle would again be ideal. It should be noted that our arguments have centered around particle numbers to this point, whereas carrier payload (volume scales with R_p^3) and maximum particle concentration also depend on size. These factors add additional optimization criteria for particle size selection. In addition, the conditions encountered within the vascular system present natural barriers that preclude the use of certain particle sizes. For example, particles larger than a few microns cannot pass through capillary beads. Furthermore, splenic filtration preferentially captures rigid particles larger than 200–500 nm, so engineering deformability can increase this threshold to an extent [24]. On the low end of the size scale, particles smaller than 20 nm are capable of passing directly into lymph nodes [25], while those less than 100–150 nm are efficiently taken up by liver hepatocytes [26,27]. Therefore, to maximize residence time within the circulation and thereby maintain effective carrier concentration levels for multiple passes of the target region, the ideal delivery carrier size range would be between 100 and 200 nm diameter [28]. The ideal particle size identified here for targeting ICAM-1 using our monoclonal antibody happens to be within this size range. Finally, the work described herein was performed using a well-defined, reconstituted system. Consequently, translation of our findings to *in vivo* settings would require consideration of numerous factors encountered within the vascular circulation. For instance, ligands such as ICAM-1 are presented on the plasma membrane of endothelial cells rather than on a flat surface, and the non-uniform topography may affect encounter frequency. Additionally,

vessel branching and physical interactions with blood components, particularly red blood cells, can effectively mix the particles in solution and provide a secondary mechanism to reach the vessel surface. This would alleviate the dependence on diffusion, improving the selectivity and total delivery potential of larger particles.

SUMMARY

In summary, we have built upon previous methods to evaluate and characterize multivalent particle adhesion to investigate the role of particle size across the nano-metric length scale. Our results indicate that size can dramatically influence both carrier recruitment efficiency and the stability of binding through the combined effects of fluid flow dependent factors that include particle transport and shear force, as well as flow-independent factors such as mass action and contact area size. Furthermore, we demonstrated how size effects can be exploited to engineer delivery carriers with optimal binding characteristics for given therapeutic applications. Based on our findings using a particular monoclonal antibody specific for ICAM-1, we conclude that particles ranging from 100 to 150 nm would provide for maximal targeting efficiency to inflamed endothelium expressing ICAM-1, as well as optimal selectivity to prevent delivery to normal tissues.

ACKNOWLEDGMENTS

We thank E. J. Johnston and A. D. Trister for technical assistance and helpful discussions. This work was supported by Unilever Research US and NSF BES-0314265.

REFERENCES

[1] Champion, J. A., Walker, A., and Mitragotri, S., *Pharm. Res.* **25**, 1815–1821 (2008).
[2] Cuenca, A. G., Jiang, H., Hochwald, S. N., Delano, M., Cance, W. G., and Grobmyer, S. R., *Cancer* **107**, 459–466 (2006).
[3] Sinha, R., Kim, G. J., Nie, S., and Shin, D. M., *Mol. Cancer Ther.* **5**, 1909–1917 (2006).
[4] Torchilin, V. P., *AAPS J.* **9**, E128–47 (2007).
[5] Haun, J. B. and Hammer, D. A., *Langmuir* **24**, 8821–8832 (2008).
[6] Shinde Patil, V. R., Campbell, C. J., Yun, Y. H., Slack, S. M., and Goetz, D. J., *Biophys. J.* **80**, 1733–1743 (2001).
[7] Yago, T., Zarnitsyna, V. I., Klopocki, A. G., McEver, R. P., and Zhu, C., *Biophys. J.* **92**, 330–342 (2007).

[8] Springer, T. A., *Cell.* **76**, 301–314 (1994).
[9] Sakhalkar, H. S., Dalal, M. K., Salem, A. K., Ansari, R., Fu, J., Kiani, M. F., Kurjiaka, D. T., Hanes, J., Shakesheff, K. M., and Goetz, D. J., *Proc. Natl. Acad. Sci. USA* **100**, 15895–15900 (2003).
[10] Eniola, A. and Hammer, D. A., *Biomaterials* **26**, 7136–7144 (2005).
[11] Muro, S., Dziubla, T., Qiu, W., Leferovich, J., Cui, X., Berk, E., and Muzykantov, V. R., *J. Pharmacol. Exp. Ther.* **317**, 1161–1169 (2006).
[12] Dustin, M. L. and Springer, T. A., *J. Cell. Biol.* **107**, 321–331 (1988).
[13] Hentzen, E. R., Neelamegham, S., Kansas, G. S., Benanti, J. A., McIntire, L. V., Smith, C. W., and Simon, S. I., *Blood* **95**, 911–920 (2000).
[14] Lomakina, E. B. and Waugh, R. E., *Biophys. J.* **86**, 1223–1233 (2004).
[15] Goldsmith, H. L. and Turitto, V. T., *Thromb. Haemost.* **55**, 415–435 (1986).
[16] Eniola, A. O., Willcox, P. J., and Hammer, D. A., *Biophys. J.* **85**, 2720–2731 (2003).
[17] Chang, K. C. and Hammer, D. A., *Biophys. J.* **76**, 1280–1292 (1999).
[18] Mody, N. A. and King, M. R., *Langmuir* **23**, 6321–6328 (2007).
[19] Hammer, D. A. and Apte, S. M., *Biophys. J.* **63**, 35–57 (1992).
[20] English, T. J. and Hammer, D. A., *Biophys. J.* **86**, 3359–3372 (2004).
[21] Goldman, A. J., Cox, R. G., and Brenner, H., *Chemical Engineering Science* **22**, 653–660 (1967).
[22] Yago, T., Wu, J., Wey, C. D., Klopocki, A. G., Zhu, C., and McEver, R. P., *J. Cell. Biol.* **166**, 913–923 (2004).
[23] Weisel, J. W., Shuman, H., and Litvinov, R. I., *Curr. Opin. Struct. Biol.* **13**, 227–235 (2003).
[24] Chen, L. T. and Weiss, L., *Blood* **41**, 529–537 (1973).
[25] Weissleder, R., Heautot, J. F., Schaffer, B. K., Nossiff, N., Papisov, M. I., Bogdanov, A. Jr., and Brady, T. J., *Radiology* **191**, 225–230 (1994).
[26] Roerdink, F., Regts, J., Van Leeuwen, B., and Scherphof, G., *Biochim. Biophys. Acta* **770**, 195–202 (1984).
[27] Braet, F., De Zanger, R., Baekeland, M., Crabbe, E., Van Der Smissen, P., and Wisse, E., *Hepatology* **21**, 180–189 (1995).
[28] Moghimi, S. M., Hunter, A. C., and Murray, J. C., *Pharmacol. Rev.* **53**, 283–318 (2001).